

# **Can NO<sub>x</sub> reduction by CO react over carbon-based single-atom catalysts at low temperatures? A theoretical study**

Jie Shi,<sup>1,2</sup> Wei Zhang,<sup>1</sup> Yuan Pu,<sup>2</sup> Hui Li<sup>\*,1</sup> Dan Wang,<sup>\*,2</sup> and Jian-Feng Chen<sup>1,2</sup>

<sup>1</sup> *Beijing Advanced Innovation Center for Soft Matter Science and Engineering, State Key Laboratory of Organic Inorganic Composites, Beijing University of Chemical Technology, Beijing 100029, China*

<sup>2</sup> *Research Center of the Ministry of Education for High Gravity Engineering and Technology, Beijing University of Chemical Technology, Beijing 100029, China*

\* Corresponding authors: Dan Wang ([wangdan@mail.buct.edu.cn](mailto:wangdan@mail.buct.edu.cn)) and Hui Li (E-mail: [hli@mail.buct.edu.cn](mailto:hli@mail.buct.edu.cn))

## Abstract

First principles studies combined with the microkinetic analysis were performed to study the reliability and reaction mechanisms of single-atom doped graphene (SADGr) materials in catalyzing  $\text{NO}_x$  reduction with CO. By screening the 3d transition metals (Sc-Zn) and group-IV elements (Si and Ge), it was found that the Ti and Co doped graphene sheets (TiGr and CoGr) respectively own excellent catalytic activities in the  $\text{NO}/\text{NO}_2$ -to- $\text{N}_2\text{O}$  and the  $\text{N}_2\text{O}$ -to- $\text{N}_2$  processes at low temperatures. Therefore, the TiGr/CoGr composite can be a promising catalyst in  $\text{NO}_x$  reduction with CO. It was further revealed the combination of adsorption energy and electronegativity was a good descriptor to predict the activation energies. The obtained results can provide useful information for rational design of carbon-based single-atom catalysts for  $\text{NO}_x$  reduction by CO at low temperatures.

**Keywords:** Computational chemistry, Multiscale modeling, Gas purification, Nitrogen oxides, Selective catalytic reduction

## Introduction

Nitrogen oxides ( $\text{NO}_x$ ) emitted by industrial processes (e.g. chemical engineering, thermal power and metallurgy) are crucial atmospheric pollutants, which affect the global environment and endanger human's health.<sup>1,2</sup> Thereby, the reduction of  $\text{NO}_x$  to harmless  $\text{N}_2$  is an important task for environmental protection. Currently, the selective catalytic reduction (SCR) of by  $\text{NH}_3$  is the most widely used technology to remove  $\text{NO}_x$ .<sup>3,4</sup> However, the import of nitrogen-containing reducing agent requires large investments and causes corrosion of equipment. The leakage of  $\text{NH}_3$  also leads to the secondary pollution.<sup>5</sup> It has been noted that in some heavy industries both CO and  $\text{NO}_x$  are simultaneously generated in the flue gas.<sup>6,7</sup> Therefore, using CO instead of  $\text{NH}_3$  to reduce  $\text{NO}_x$  has been considered as an attractive amino-free strategy to remove both

harmful NO<sub>x</sub> and another important pollutant CO. Another advantage of using CO as a reducing agent is the avoidance of carbon deposition and corrosion of equipment.<sup>8-10</sup> To date, a series of catalysts based on noble metals<sup>3,8,11</sup> and/or transition metals<sup>12,13</sup> on the substrates of metal oxides or zeolites have been applied as efficient NO<sub>x</sub> reduction catalysts. However, the massive metal consumption makes them not sustainable in the long run. Furthermore, such kinds of catalysts usually exhibit low performance in CO-SCR at low temperatures (< 300 °C).<sup>14,15</sup> Therefore, development of carbon based catalysts with little or no metals for NO<sub>x</sub> reduction at low temperatures will have important implications on satisfying the sustainable development theory.

Recent advances in nanotechnologies and material science enable researchers to explore tremendous novel nanostructured catalysts of single-atom catalysts (SACs) with extraordinary catalysis properties due to the 100% atom utilization efficiencies.<sup>16-19</sup> Among them, the single-atom-doped graphene (SADGr) has become one of the hotspots for the ease of access and harmlessness to the environment.<sup>20,21</sup> Experimentally, the SADGr materials have been reported as electrode materials and thermal reaction catalysts.<sup>22-25</sup> Theoretical studies based on density functional theory (DFT) simulations have demonstrated that heteroatom-doped graphene has good adsorption/dissociation ability for NO<sub>x</sub>.<sup>26,27</sup> However, there have been no systematic studies on carbon-based single-atom catalysts for NO<sub>x</sub> reduction by CO.

In this work, the feasibility and the possible mechanisms of NO<sub>x</sub> reduction with CO catalyzed by graphene sheets doped by the 3d TM (Sc, Ti, V, Cr, Mn, Fe, Co, Ni, Cu, and Zn) and group-IV (Si, Ge) elements were investigated through first principles studies combined with the microkinetic analyses and molecular dynamics (MD) simulations. It was found the Ti-doped graphene (TiGr) possessed the excellent activity in NO reduction to N<sub>2</sub>O at 450 K, while the Co-doped graphene (CoGr)

exhibited effective conducive in  $\text{N}_2\text{O}$  reduction. Both catalysts showed high stability under the reaction conditions. Thereby, the TiGr and CoGr combo-catalysis could be an efficient candidate for  $\text{NO}_x$  reduction with CO at low temperatures. It is further revealed the combination of gas adsorption energy and catalyst electronegativity is a great descriptor for the free energy barriers of key steps in the catalytic reactions, thereby providing a simple method for the design of SACs.

## Computational methods

### *DFT simulation setup*

The first principles calculations are performed within the framework of density functional theory (DFT) using the Vienna ab initio simulation package (VASP).<sup>28</sup> The reparametrized Perdew–Burke–Ernzerhof (revPBE) functional is employed to calculate the exchange and correlation energies,<sup>29</sup> combined with the Rutgers-Chalmers van der Waals Density Functional (vdw-DF),<sup>30</sup> in order to more accurately describe the dispersion interactions between the adsorbate and the surface. The wavefunctions are described by a plane-wave basis set ( $E_{\text{cutoff}} = 450$  eV) and the projected augmented wave (PAW) pseudopotential. A  $4 \times 8$  supercell of graphene sheet (composed of 64 atoms) doped by one single atom is used as the catalyst model with a 20 Å vacuum distance to eliminate the periodic image interaction. In the electronic structure calculation, the first Brillouin zone (BZ) is sampled by a  $2 \times 1 \times 1$  Monkhorst–Pack k-mesh, and only Gamma point is used in the ab-initio Molecular Dynamics (AIMD) simulations. Structural optimizations are carried out until the maximum atomic force is  $< 0.01$  eV/Å. The localized 3d electrons correlation for transition metal in fourth period can be generally described by considering on-site coulomb ( $U$ ) and exchange ( $J$ ) interactions. Here, we applied the DFT +  $U$  calculations through the rotationally invariant approach<sup>31</sup> with the corresponding  $U - J$  values for Ti and Co shown in Fig. S2.

The climbing image nudged elastic band method (CI-NEB)<sup>32</sup> is employed to search for the transition states and minimum energy paths (MEP) for the reduction reactions. The spring force between adjacent images is set to 5.0 eV/Å and images are initially optimized until the forces on each atom are less than 0.10 eV/Å. After that, the exact location of the saddle point is found by refining the estimate with the dimer method,<sup>33</sup> and thereby the activation energy barrier can be calculated. The criterion force for the transition state is also 0.01 eV/Å.

The ab-initio molecular dynamics (AIMD) simulations, including annealing and constrained MD, are also carried out to confirm the reaction paths from NEB calculations as well as the stability of catalysts under reaction conditions. The timestep is 1.0 fs, and the heating rate of annealing method is 0.1 K/fs. The potential of mean force (PMF) of constrained MD is calculated for deriving the Helmholtz free energy surface, based on the slow-growth method proposed by Michiel Sprik.<sup>34</sup> The collective variables (CVs) used to explore the CO oxidation process are set as the difference between the distance of O\*-D (dopant atom) and the distance of C-O\*. Generally, AIMD simulations for 5-10 ps are performed to collect the mean force on the reaction coordinate (the O\*-D distance minus the C-O\* distance) to obtain the CO oxidation free energy. The CVs of other processes are explained in the figure captions.

The Gibbs free energy  $G(T)$  of each state is estimated through  $G(T) = U(T) + pV - TS$ , in which the zero-point correction ( $\Delta ZPE$ ) and the  $pV$  contribution of gaseous molecules at 1 atm are included in the free energy correction. The thermodynamic correction data are obtained from the VASPKIT package.<sup>35</sup> The adsorption free energy ( $\Delta G_{ads}$ ) on the catalyst surface is calculated by

$$\Delta G_{ads} = G_{total} - G_{adsorbate} - G_{catalyst}, \quad (1)$$

where  $G_{total}$ ,  $G_{adsorbate}$ , and  $G_{catalyst}$  represent the total free energy, the free energy of isolated atom/molecule, and the free energy of bare catalyst, respectively. Similarly, the formation free energy  $\Delta G_{form}$  of  $(NO)_2^*$  is calculated by

$$\Delta G_{form} = G_{total} - n \times G_{monomer-ads} - G_{catalyst}, \quad (2)$$

where  $G_{NO}$  is the free energy of isolated NO monomer. The reaction free energy ( $\Delta G_r$ ) of one process is calculated by

$$\Delta G_r = G_{FS} - G_{IS}, \quad (3)$$

where  $G_{IS}$  and  $G_{FS}$  denote the free energies of the initial and final states, respectively. The activation free energy barrier ( $\Delta G_b$ ) is estimated according to

$$\Delta G_b = G_{TS} - G_{IS}, \quad (4)$$

where  $G_{TS}$  and  $G_{IS}$  denote the energies of the transition and initial states, respectively.

### ***Functional benchmark.***

In order to ensure accuracy and efficiency of the computational method in this work, the cohesive/adsorption energies and magnetic moments of Group-IV elements (Si and Ge) doped graphene and gas-adsorption structures on SiGr derived from three different functionals (PBE, vdw-DF, and HSE06<sup>36</sup>) are compared. As listed in Table S1, the three different functionals provide consistent magnitudes of cohesive/adsorption energies of Si/Ge/O-doped graphene and adsorption structures. The calculated magnetic moments from the vdw-DF and HSE06 are also identical, but inconsistent to the PBE results (D2 and D3 in Table S1). Since it is widely accepted the HSE06 hybrid functional is usually more reliable in electronic structure calculation but too computational expensive for transition state optimization, the vdw-DF functional is employed in all the subsequent calculations.

### ***Microkinetic model***

The steady-state microkinetic model is used to derive the surface concentrations of all reaction intermediates to quantify the reaction rate contribution of each reaction step. According to the collision theory, the reaction rate constant ( $k_i$ ) of the adsorption or collision processes can be obtained through

$$k_i = \frac{\sigma}{\sqrt{2\pi m_A k_B T}} \exp\left(-\frac{\Delta G_{bi}}{k_B T}\right) \quad (5)$$

where  $\sigma$  is the average area of an active center, the same size of the SADGr unit cell ( $\sigma = 1.68 \times 10^{-18} \text{ m}^2$ ). The other parameters are the mass of the adsorbed molecule  $m_A$ , the activation free energy of reaction  $\Delta G_{bi}$  (If there is no energy barrier in the adsorption process, it is set as 0.), Boltzmann's constant  $k_B$ , and the temperature  $T$ . Based on the transition state theory, the rate constant ( $k_i$ ) of the dissociation or desorption steps can be obtained by

$$k_i = \frac{k_B T}{h} \exp\left(-\frac{\Delta G_{bi}}{k_B T}\right) \quad (6)$$

where  $h$  denotes the Planck constant. The reaction equilibrium constant ( $K_i$ ) is calculated by

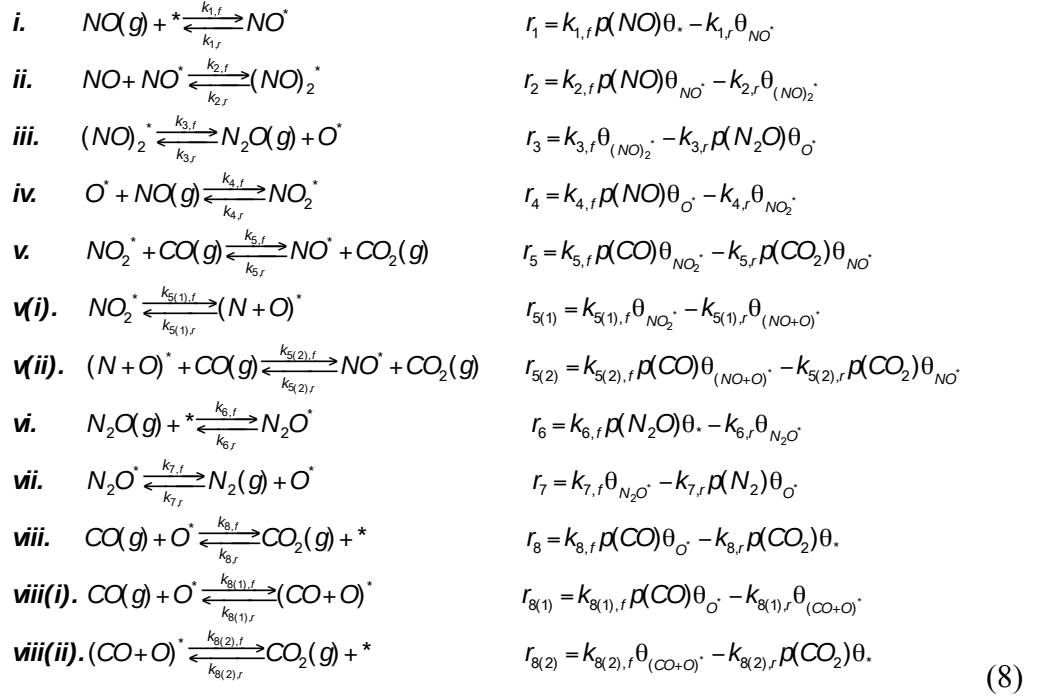
$$K_i = \frac{k_{i,f}}{k_{i,r}} = \exp\left(-\frac{\Delta G_{bi,f} + \Delta G_{bi,r}}{k_B T}\right) \quad (7)$$

where  $k_{i,f}$  and  $k_{i,r}$  respectively correspond to the rate constants of the forward and backward reactions.

In the microkinetic simulation, the reaction temperature is set to 450 K, the total gas pressure is set as 1 atmosphere, the content of NO and N<sub>2</sub>O is set as 1000 ppm, the content of CO is set as 1%, and the content of CO<sub>2</sub> is set as 20%. In the case of varying the partial pressures of NO and CO to study TiGr activity, the contents of the other gas components remain unchanged. When studying the CoGr activity with varying CO partial pressure, the NO content is set as 10 ppm. In the study the activity of TiGr in catalyzing the reduction of N<sub>2</sub>O by changing the partial pressure of N<sub>2</sub>O, the NO and CO contents are set as 100 ppm and

10%, respectively. The details of microkinetic model for NO<sub>x</sub> reduction by CO are given in the Computational methods section.

The microkinetic model of NO<sub>x</sub> reduction by CO is established, as shown by



(8)

where  $\theta_* + \theta_{NO^*} + \theta_{(NO)_2^*} + \theta_{O^*} + \theta_{NO_2^*} + \theta_{(NO+O)^*} + \theta_{N_2O^*} + \theta_{(CO+O)^*} = 1$ .

Based on the steady-state model, the generation and consumption rates of each surface specie are equal, so the coverage of surface adsorbed species and the reaction rate of each step can be obtained as

$$\begin{aligned}
 \frac{\partial \theta_*}{\partial t} &= -r_1 - r_6 + r_8 = 0 & \frac{\partial \theta_{NO^*}}{\partial t} &= r_1 - r_2 + r_5 = 0 & \frac{\partial \theta_{(NO)_2^*}}{\partial t} &= r_2 - r_3 = 0 \\
 \frac{\partial \theta_{O^*}}{\partial t} &= r_3 - r_4 + r_7 - r_8 = 0 & \frac{\partial \theta_{NO_2^*}}{\partial t} &= r_4 - r_5 = 0 & \frac{\partial \theta_{N_2O^*}}{\partial t} &= r_6 - r_7 = 0
 \end{aligned} \quad (9)$$

## Results and discussion

### Structures and stabilities of catalysts

In the last decade, numerous atom-doped graphene materials (e.g. B, N, O, Si, P, S, Fe, Mo, Ag, etc.) have been experimentally synthesized,<sup>23-25,37,38</sup> and it is worth noting that the TM-SADGr models have been widely reported as electrochemical reaction catalysts by DFT



researches.<sup>39,40</sup> For the low temperature NO<sub>x</sub> reduction, we build models of single-atom-doped graphene (SADGr) by replacing a C atom with a single metal atom (Fig. 1(a)). Based on the functional benchmark (see details in Computational methods and Table S1 in the supporting information, SI), the vdW-DF functional exhibits a good balance between high accuracy and moderate computational cost, thereby is employed in all calculations in the present work. As shown in Fig. 1(b), the large cohesive energies respecting to both the defected graphene ( $E_c(\text{SiGr}) = 7.83 \text{ eV}$ ;  $E_c(\text{GeGr}) = 5.96 \text{ eV}$ ) and the bulk forms of Si and Ge ( $\Delta E_c(\text{SiGr}) = 3.48 \text{ eV}$ ;  $\Delta E_c(\text{GeGr}) = 2.48 \text{ eV}$ ) demonstrate the high thermodynamic stability of both Group-IV elements doped graphene sheets. Similarly, except CuGr and ZnGr, all the other 3d TM-doped graphene materials are also provided with significantly larger cohesive energies relative to bulk forms ( $\Delta E_c(\text{TMGr}) = 1.32 \sim 3.48 \text{ eV}$ , TM = Sc, Ti, V, Cr, Mn, Fe, Co, and Ni), indicating such doped graphene materials are highly stable, which can be easily obtained by deposition of dopant substances on defected graphene. In addition, the high stability of SADGr materials in the reaction environment ( $T = 450 \text{ K}$ ) are further verified by the AIMD simulations in the subsequent discussions of reaction processes.

### ***Reaction mechanisms***

Since the (NO)<sub>2</sub> dimer firstly characterized by infrared spectroscopy, (NO)<sub>2</sub> has been widely found in gas-solid catalytic systems. Extensive studies also pointed out the energy barrier for direct dissociation of NO molecule is greater than the barrier for NO reduction with the assistance of other molecules or active species<sup>14,41</sup>. Here, the reduction of NO on the surface of SADGr is found to adopt the similar NO dimerization mechanism. As shown in Fig. 1(c), all reactions involved in the catalytic reduction of NO<sub>x</sub> by CO can be divided into three cycles, where the red, blue, and orange cycles represent the reduction process of NO to N<sub>2</sub>O (No. 1), the generation and reduction processes of NO<sub>2</sub> to NO (No. 2), as well as the reduction process of N<sub>2</sub>O

to N<sub>2</sub> (No. 3), respectively. The 1<sup>st</sup> cycle includes four elementary steps, as shown by i, ii, iii, and viii in Fig. 1(c). The 2<sup>nd</sup> cycle includes steps ii, iii, iv, and v, while the 3<sup>rd</sup> cycle includes steps vi, vii, and viii. It is worth noting that, depending on the activity of catalyst, the step v can be respectively divided into v(i), where NO<sub>2</sub> dissociates and forms the co-adsorption (NO+O)\* on the dopant atom, and v(ii), where the co-adsorption (NO+O)\* is reduced by CO to NO\* and CO<sub>2</sub>. Similarly, the step viii can be divided into viii(i), where CO and O\* form a co-adsorption structure of (CO+O)\* first, and viii(ii), where CO\* is oxidized by O\* to CO<sub>2</sub>. In the whole catalytic reaction, an efficient catalyst needs to conduct at least one reaction cycle and avoid being poisoned by other substances in the reaction environment.

### ***NO<sub>x</sub> Reduction***

Since the gas adsorption is the key step of in the whole reaction on catalyst surfaces, we firstly compare the adsorption structures and free energies  $\Delta G_{\text{ads}}$  of all the gaseous chemical species (NO, CO, (NO)<sub>2</sub>, N<sub>2</sub>O, O, and NO<sub>2</sub>) involved in the NO<sub>x</sub> reduction. The values of  $\Delta G_{\text{ads}}$  are estimated by including the entropy of the gaseous and adsorbed molecules, as well as the  $pV$  contribution ( $p = 1 \text{ atm}$ ) from the gaseous molecules (see details in Computational methods). Fig. 2(a) displays  $\Delta G_{\text{ads}}$  (the maximum absolute values) of some key adsorbed species in the catalytic reactions. The magnitudes of  $\Delta G_{\text{ads}}$  and adsorption structures of all the gaseous species are respectively listed in Table S2-S6 and shown in Fig. S1, SI. Except for the GeGr ( $\Delta G_{\text{ads}} = 0.406 \text{ eV}$ ), NO can strongly adsorb on SADGr sheets ( $\Delta G_{\text{ads}} = -0.45 \sim -1.53 \text{ eV}$ ). Depending on the properties of SADGr surfaces, the NO can adopt three kinds of stable adsorption configurations: the N-adsorption (N<sub>ad</sub>O) structure, the O-adsorption (NO<sub>ad</sub>) structure, and the lying structure with both N and O attached to the dopant (N<sub>ad</sub>O<sub>ad</sub>), as shown in Fig. S1(a-c). By contrast, the adsorbed CO can form only one

stable configuration with the C atom pointing to the dopants (Fig. S1(d)). The relative higher adsorption free energies of CO ( $\Delta G_{\text{ads}} = -0.54 \sim 0.59$  eV) indicate the adsorption of CO is much less preferable than NO. The (NO)<sub>2</sub> dimer can also take three alternative adsorption configurations on the dopant denoted by D1, D2, and D3, as shown in Fig. S1(f-h). D1 and D3 are the cis-(NO)<sub>2</sub> species chemisorbed on the doping atom in form of O<sub>ad</sub>NNO<sub>ad</sub>, and ON<sub>ad</sub>N<sub>ad</sub>O, respectively, while D2 is a trans-(NO)<sub>2</sub> specie in form of ON<sub>ad</sub>NO<sub>ad</sub>. As shown in Fig. 2(a) and listed in Table S4, the formation free energies of adsorbed (NO)<sub>2</sub> dimers are generally in the order of  $\Delta G(\text{D1}) < \Delta G(\text{D3}) < \Delta G(\text{D2})$ . In addition, we also carried out the PBE+*U* calculations on the adsorption of key species on TiGr and CoGr, which provide consistent adsorption energies with the conventional PBE results, as shown in Fig. S2. Therefore, the calculations in this work are performed without considering the on-site coulomb (*U*) and exchange (*J*) interactions.

### **NO reduction**

Although D1 is the most energetically stable adsorption structure of (NO)<sub>2</sub>, its formation requires the previously adsorbed NO monomer converting from the N<sub>ad</sub>O structure to the relatively unstable NO<sub>ad</sub> structure. For adsorption processes, the energy barriers of D1 formation are usually large ( $\Delta G_b = 0.26 \sim 1.05$  eV), as depicted by the energy profiles (black lines) in Fig. 3(a-h & k-l). On the other hand, D2 and D3 can be spontaneously formed from the N<sub>ad</sub>O structure and transformed into each other under thermal fluctuations. Therefore, D2 and D3 are kinetically favorable to form on the SADGr surfaces (except CuGr and ZnGr). It is further found D2 and D3 can easily dissociate into adsorbed O\* and gaseous N<sub>2</sub>O through small barriers (for a decomposition reaction,  $\Delta G_b = 0.28 \sim 0.88$  eV, except for VGr, CrGr and MnGr), as shown by the energy profiles (red lines) in Fig. 3(a-h & k-l). The thermodynamically

optimal values of forward and backward  $\Delta G_b$  of  $(\text{NO})_2$  decomposition are also depicted in Fig. 2(c). The spontaneous formation of the  $(\text{NO})_2$  on TiGr and SiGr indicated by the nudged elastic band (NEB) calculations are further confirmed by the ab-initio molecular dynamics (AIMD) simulations at 450 K (Fig. S3-S4). As shown in Fig. S5, the AIMD simulations are performed to discuss the thermal stability of all 12 types SADGr catalysts in NO atmosphere at 450 K. It is found that except for the escape of Zn atom from the defect of ZnGr during the simulation process, other SADGr exhibits excellent stability in the NO atmosphere.

### **NO<sub>2</sub> reduction.**

It is known NO<sub>x</sub> mixture usually contains a small amount of NO<sub>2</sub>, which can competitively adsorb on the exposed dopant sites. In addition, NO<sub>2</sub>\* can be easily formed by adsorbing a NO molecule from the gas phase on the O\* remained from  $(\text{NO})_2$  reduction or N<sub>2</sub>O reduction. As shown in Fig. S1(k-m), the adsorbed NO<sub>2</sub> can adopt three alternative structures, named as NO<sub>2</sub>-ads1 (O<sub>ad</sub>NO), NO<sub>2</sub>-ads2 (O<sub>ad</sub>N<sub>ad</sub>O), and NO<sub>2</sub>-ads3 (O<sub>ad</sub>NO<sub>ad</sub>), with large adsorption energies ( $\Delta G_{\text{ads}} = -0.28 \sim -2.30$  eV, Table S5). Thus, in order to prevent catalyst poisoning, removing NO<sub>2</sub>\* from the catalyst surface is crucial for NO reduction. The elimination of NO<sub>2</sub>\* may follow two possible paths: endothermic decomposition back to NO(g) and O\*, or reduction by CO(g) to NO\* and CO<sub>2</sub>(g). The process of NO<sub>2</sub>\* reduction by CO demonstrates two situations, as shown in Fig. 4. On the highly coordinatively unsaturated metal site (Number of d electrons  $\leq 8$ ), the adsorbed NO<sub>2</sub> is first decomposed into (NO+O)\* co-adsorbed on the same site (step v(i) in Fig. 1(c)), and then reduced by CO. This process requires NO<sub>2</sub>\* to undergo the NO<sub>2</sub>-ads2 configuration and break the N<sub>ad</sub>-O<sub>ad</sub> bond. However, on the dopants with fewer empty orbitals, including CuGr, ZnGr, SiGr, and GeGr, NO<sub>2</sub>\* is directly reduced to NO\* under the collision of CO without undergoing the dissociation process. It is

worth noting that, on the SADGr surfaces (except ZnGr), the energy barrier of the reverse reaction of step iv ( $\Delta G_{b,r} = 0.04 \sim 1.30$  eV) is smaller than the forward barrier of step v ( $\Delta G_{b,f} = 0.91 \sim 1.61$  eV) as Fig. 2(c). So the  $\text{NO}_2^*$  tends to decompose into  $\text{NO(g)} + \text{O}^*$ , which can prevent these catalysts from being poisoned by  $\text{NO}_2$  and shift the reaction to the easy process ( $\text{O}^* + \text{CO(g)} \rightarrow \text{CO}_2\text{(g)} + *$ ).

### **$\text{N}_2\text{O}$ reduction**

The product  $\text{N}_2\text{O}$  in  $(\text{NO})_2$  reduction can be further reduced to harmless  $\text{N}_2$ . Among the SADGr materials, MnGr and CoGr are found to possess very high activity for  $\text{N}_2\text{O}$  reduction, where  $\text{N}_2\text{O}$  can strongly adsorb and dissociate to  $\text{N}_2\text{(g)}$  and  $\text{O}^*$  (step vi and vii in Fig. 1(c)) without any barrier, as shown in Fig. 5. The spontaneous reduction processes on both surfaces are also reproduced by the AIMD simulation (Fig. S6-S7). Furthermore, VGr ( $\Delta G_{\text{ads}} = -0.17$  eV) and CrGr ( $\Delta G_{\text{ads}} = -0.05$  eV) show weak attraction to  $\text{N}_2\text{O}$  as listed in Table S6, forming the  $\text{N}_{\text{ad}}\text{NO}$  structure with the N atom approaching to the dopant. By contrast, the positive adsorption free energies indicate  $\text{N}_2\text{O}$  cannot stably adsorb on remaining SADGr surfaces, where the reduction can only occur through the ER mechanism. All the reduction barriers of step vi and vii are shown in Fig. 2(c).

### ***CO Oxidation***

The remained  $\text{O}^*$  atoms from the reduction of  $(\text{NO})_2$  and  $\text{N}_2\text{O}$  can strongly chemisorb on the SADGr surfaces ( $\Delta G_{\text{ads}} = -0.27 \sim -2.76$  eV, Table S6), leading to the poisoning of catalytic sites. Thus, the next key step of catalytic reduction of  $\text{NO}_x$  is to employ CO to take away the adsorbed O atoms. The energy profiles of reaction paths for CO oxidized by  $\text{O}^*$  are shown in Fig. 6. It is found the formation of CO and O co-adsorption structure ( $((\text{CO} + \text{O})^*)$ ) on the single-atom sites covered by  $\text{O}^*$  (step viii(i) in Fig. 1(c)) is energetically unfavorable, only except for ScGr, indicating the CO

oxidation with O\* is usually following the ER mechanism. Furthermore, although VGr and MnGr exhibit great activity in NO<sub>x</sub> reduction, the CO oxidations on both surfaces are endothermic or slightly exothermic ( $\Delta G_r = 0.34$  eV and  $-0.07$  eV, respectively), attributing to the formation of strong O-V and O-Mn bonds. As a result, it is difficult to remove O\* from both surfaces, leading to the poisoning of the catalysts. The CO oxidation processes obtained from the NEB calculations are also confirmed by the constrained AIMD simulations, where both the free energy surfaces and intermediate structures of the CO oxidation reaction are well reproduced (Fig. S8-S19).

### ***Microkinetic analysis***

Based on the energy barriers obtained from DFT, we employ the transition state theory and the steady-state microkinetic analysis to quantitatively predict the reaction rate, presented by the turn-over frequencies (TOFs), as well as the surface concentrations of adsorbed species to evaluate the performance of catalysts under the real reaction conditions (see Computational methods section). As listed in Table S7, the forward reaction rate constants of steps v and viii are relatively small ( $k_{5,f} = 3.68 \times 10^{-14} \sim 2.53 \times 10^{-6} \text{ Pa}^{-1} \cdot \text{s}^{-1}$  and  $k_{8,f} = 1.43 \times 10^{-7} \sim 1.64 \text{ Pa}^{-1} \cdot \text{s}^{-1}$ ), due to the low adsorption ability of CO and the nonnegligible energy barriers in the oxidation reactions. By combining the backward reaction rate constants (Table S8), the reaction equilibrium constants ( $K_i$ ) are derived, as listed in Table S9. Except for VGr ( $K_8 = 2.15 \times 10^{-4}$ ) and MnGr ( $K_8 = 7.23$ ), the equilibrium constants of key reaction steps ( $K_3$ ,  $K_5$ ,  $K_7$ , and  $K_8$ ) are usually far greater than 1, indicating the NO<sub>x</sub> reduction by CO is thermodynamically favorable on most SADGr surfaces.

The forward and backward rates of each reaction step are calculated in the atmosphere with the gas concentrations of 0.1% NO and 1% CO at 450 K, as listed in Table S10-

S11. As shown in Figs. 7(a) and S20, the TiGr holds the highest TOFs of  $1.8 \times 10^{-2}$  and  $3.4 \times 10^{-4} \text{ s}^{-1}$  in reaction cycles 1 and 2, respectively, followed by FeGr, VGr, SiGr, on which the TOFs in cycle 1 are  $2.0 \times 10^{-3}$ ,  $7.1 \times 10^{-4}$ , and  $3.2 \times 10^{-4} \text{ s}^{-1}$ , respectively. However, all these four most active catalysts in cycle 1 show low efficiency in cycle 3, where  $\text{N}_2\text{O}$  is hardly reduced to  $\text{N}_2$ . By contrast, the  $\text{N}_2\text{O}$  reduction is barrierless on MnGr and CoGr, although both catalysts do not possess high activity in cycles 1 and 2. According to the microkinetic results, although most catalytic sites of TiGr surface are occupied by O and  $\text{NO}_2$  (Figs. 7(b) and S21), the large reverse rate of step iv indicates the  $\text{NO}_2^*$  can rapidly decompose into  $\text{O}^*$  and  $\text{NO}(\text{g})$ , preventing the catalyst from being poisoned by  $\text{NO}_2$ . Thereby, the removal rate of  $\text{O}^*$  is the rate-determining step on TiGr. Similarly, many catalysts (including VGr, MnGr, FeGr, CoGr, NiGr, and SiGr) are found to have good performance in the reaction cycles 1 or 3 with relatively large reverse rates of step iv. However, these surfaces are all covered with a certain concentration of  $\text{O}^*$ , indicating the CO oxidation is the rate-determining step for these SADGr catalysts. It is further proved that the small forward and reverse reaction rates caused by the large reduction and dissociation energy barrier make ScGr and CrGr easily poisoned by  $\text{NO}_2$  and  $(\text{NO})_2$  at 450 K.

Since TiGr owns the highest activity in the reaction of NO reduction by CO, the influence of NO and CO partial pressures on its catalytic ability is further studied, as shown in Fig. 7(c). The TOF of step viii presents positive and negative relations with  $P_{\text{NO}}$  and  $P_{\text{CO}}$ , respectively. Under the conditions of exhaust gas, where  $P_{\text{NO}}$  and  $P_{\text{CO}}$  respectively equal to 1.01 Pa (10 ppm) and  $1.01 \times 10^4$  Pa (10.0%), the TOF value can reach  $\sim 0.5 \text{ s}^{-1}$ . Furthermore, the reaction rate of step vii is also increased due to the increasing  $P_{\text{N}_2\text{O}}$  during the NO reduction (Fig. S22). However, such reaction rate ( $\text{TOF} = 10^{-7} \sim 10^{-4} \text{ s}^{-1}$ ) is negligible compared to the rates of steps iii and viii, therefore has

no detectable effect on the total reaction rate. Similarly, the effect of  $P_{\text{CO}}$  on the reaction rates ( $P_{\text{NO}}$  equals to 1.01 Pa) is also discussed on CoGr, the most active catalyst in cycle 3, as shown in Fig. 7(d). By increasing the CO concentration from 1% to 10 %, the reaction rates of steps vii and viii in cycle 3 is enhanced from  $3.5 \times 10^{-4}$  to  $3.5 \times 10^{-3} \text{ s}^{-1}$ , while the incidences of side reactions in cycles 1 and 2 remain extremely low (TOFs  $< 10^{-7} \text{ s}^{-1}$ ). Thus, the combination of TiGr and CoGr in a sequence is the most efficient catalyst to reduce  $\text{NO}_x$  to  $\text{N}_2$  with CO. It is worth noting the TOF values of TiGr for NO reduction and CoGr for  $\text{N}_2\text{O}$  reduction can respectively reach  $1.8 \times 10^{-2}$  and  $3.5 \times 10^{-4} \text{ s}^{-1}$  at  $\sim 180^\circ\text{C}$ , which are comparable to the activity of commercial  $\text{V}_2\text{O}_5/\text{TiO}_2$  catalyst in the traditional  $\text{NH}_3$ -SCR (TOFs =  $1.3 \times 10^{-3} \text{ s}^{-1}$  at  $277^\circ\text{C}$ <sup>42</sup> and  $2.4 \times 10^{-3} \text{ s}^{-1}$  at  $323^\circ\text{C}$ <sup>43</sup>). We also explore the sensitivity of the reaction rate to the energy barrier of a non-rate-determining step. For instance, on the TiGr surface (Fig. S23), the energy barrier of step iii is not provided with a significant impact on the total rate until it is greater than 1 eV. According to the surface concentrations, until the energy barrier of step iii becomes  $> 1.2 \text{ eV}$ , the concentration of  $\text{NO}^*$  can exceed it of  $\text{O}^*$  or  $\text{NO}_2^*$ , leading to the change of rate-determining step (Fig. S23).

### ***Structure-activity descriptors***

It is known the adsorption strength of key species is often related to the reaction activity in thermal catalytic reaction. Here, it is revealed that the combination of adsorption energy and electronegativity (Table. S12), another important indicator for the interaction between reactants and catalytic sites, can be a good descriptor for the activity of the  $\text{NO}_x$  reduction as following:

$$\varphi = c \times \frac{-\sum (\Delta G_{\text{ads}}(R) - \Delta G_{\text{ads}}(P))}{\sum_1^n (E(R) - E(P_i)) / n - E(D)} \quad (10)$$



where  $\Delta G_{\text{ads}}(\text{R})$  and  $\Delta G_{\text{ads}}(\text{P})$  represent the adsorption energies of key species involved in reactants and products,  $E(\text{R})$ ,  $E(\text{P})$  and represent the electronegativities of the atoms in key species in reactants and products and  $E(\text{D})$  represents the electronegativity of the dopant atom,  $n$  is the net number of atoms in key species and  $c$  is the correction coefficient. As displayed in Fig. 8, except for the  $\text{N}_2\text{O}$  reduction, the energy barriers of all the other three processes can be well fitted, where descriptors of NO reduction ( $\varphi_{\text{NO}}$  in Fig. 8(a)),  $\text{NO}_2$  reduction ( $\varphi_{\text{NO}_2}$  in Fig. 8(b)), and CO oxidation ( $\varphi_{\text{CO}}$  in Fig. 8(d)) are calculated as:

$$\varphi_{\text{NO}} = -\frac{\Delta G_{\text{ads}}(\text{NO})}{n} \quad (11)$$

$$\varphi_{\text{NO}_2} = 2 \times \frac{-(\Delta G_{\text{ads}}(\text{NO}_2) + \Delta G_{\text{ads}}(\text{CO}) - \Delta G_{\text{ads}}(\text{O}))}{((E_{\text{N}} + 2E_{\text{O}} + E_{\text{C}} - E_{\text{O}})/3 - E_{\text{D}})} \quad (12)$$

$$\varphi_{\text{CO}} = 0.5 \times \frac{-(\Delta G_{\text{ads}}(\text{O}) + \Delta G_{\text{ads}}(\text{CO}))}{((E_{\text{O}} + E_{\text{C}})/2 - E_{\text{D}})} \quad (13)$$

It is worth noting that the fitting of CuGr and ZnGr is significantly biased by  $\varphi_{\text{NO}_2}$ , due to the fact that  $\text{NO}_2^*$  does not decompose into  $(\text{NO}+\text{O})^*$  on both surfaces and reacts with CO in a different path from other catalysts. The increase in the CO oxidation barriers ranging from FeGr to CoGr is attributed to the difficulty of forming the transition state  $(\text{C}_{\text{ad}}\text{O}-\text{O}_{\text{ad}})^*$  structure on the post-transition element. For the description of the barrier of the CO oxidation, we also try to conduct a charge density difference analysis (Fig. S24). It can be found, to a certain extent, the greater the amount of electrons transfer from the dopant atom to  $\text{O}^*$ , the easier it is for  $\text{O}^*$  to oxidize CO. On the other hand, due to the weak adsorption of  $\text{N}_2\text{O}$  and the low energy barrier in the reaction process, there are no obvious trends of change, the descriptor  $\varphi_{\text{N}_2\text{O}}$  cannot fit the  $\text{N}_2\text{O}$  reduction well (Fig. 8(c)):

$$\varphi_{\text{N}_2\text{O}} = \frac{-(\Delta G_{\text{ads}}(\text{N}_2\text{O}))}{((2E_{\text{N}} + E_{\text{O}})/3 - E_{\text{D}})} \quad (14)$$

In addition to the adsorption energy and electronegativity, the charge distribution of a single-atom catalyst can be used to simply predict its adsorption performance for key species.<sup>44</sup> As shown in Fig. 9, the relationships between the Bader charges of active site of SADGr catalysts and the adsorption free energies of key species (NO, CO, NO<sub>2</sub>, O) are derived. Since the adsorption of N<sub>2</sub>O is weak on almost all SADGr surfaces, it is not considered in the descriptors. With the increase of the Bader charge, the adsorption of key species shows a volcanic trend of first strengthening and then decreasing. Therefore, the not-strong-not-weak adsorption of TiGr and CoGr is relevant to the location of the volcanic mountainside formed by the trend line in Fig. 9. Overall, according to the charge of the active sites of the catalyst, it may not be possible to accurately predict the activity of the catalyst, but qualitatively, it helps us analyse the adsorption performance and exclude some bad catalysts, which own too strong or too weak adsorption to reactive species.

## Conclusions

In summary, by using DFT calculations combined with microkinetic analysis and AIMD simulations, we explore the reliability and mechanisms of the single-atom-doped graphene (SADGr) catalytic reduction of NO<sub>x</sub> with CO at 450 K. The systematic research on 3d transition metals (Sc-Zn) and two group-VI elements (Si and Ge) doped graphene materials indicates that the TiGr holds an excellent catalytic activity in the reaction cycle of CO reducing NO/NO<sub>2</sub> to N<sub>2</sub>O, while the CoGr is good at reducing N<sub>2</sub>O to N<sub>2</sub>. Both the carbon-based single-atom catalysts are stable under the reaction conditions. The predicted TOFs of both catalysts are comparable to the commercial V<sub>2</sub>O<sub>5</sub>/TiO<sub>2</sub> catalyst in traditional NH<sub>3</sub>-SCR, indicating the TiGr/CoGr composite can be a promising catalyst to reduce NO<sub>x</sub> to N<sub>2</sub> with CO. In addition, it is also revealed the combination of adsorption energy and electronegativity can act as a good descriptor to predict the activation energy of the catalytic

reaction. The present study gives a comprehensive theoretical understanding of the stability, activity, and selectivity of SADGr catalysts to realize the NO<sub>x</sub> reduction with CO, and provides important guidance for experimental and theoretical designs of novel green and efficient NO<sub>x</sub> removal catalysts.

## Acknowledgements

This work was partially supported by the National Natural Science Foundation of China (21773005, 21935001, 91934303, 21620102007). We are also grateful for the support by the High Performance Computing Platform of BUCT.

## References

1. Liu J, Liu J, Zhao Z, Wei Y, Song W. Fe-Beta@CeO<sub>2</sub> core-shell catalyst with tunable shell thickness for selective catalytic reduction of NO<sub>x</sub> with NH<sub>3</sub>. *AIChE J.* 2017;63:4430-4441.
2. Wang P, Yi J, Sun C, Luo P, Lei L. Evaluation of H<sub>2</sub> influence on the evolution mechanism of NO<sub>x</sub> storage and reduction over Pt-Ba-Ce/ $\gamma$ -Al<sub>2</sub>O<sub>3</sub> catalysts, *Engineering* 2019;5: 568-575.
3. Gholami Z, Luo G, Gholami F, Yang F. Recent advances in selective catalytic reduction of NO<sub>x</sub> by carbon monoxide for flue gas cleaning process: a review. *Cat. Rev.* 2020:1-52.
4. Song L, Ma K, Tian W, Ji J, Liu C, Tang S, Jiang W, Yue H, Liang B. An environmentally friendly FeTiSO<sub>x</sub> catalyst with a broad operation-temperature window for the NH<sub>3</sub>-SCR of NO<sub>x</sub>. *AIChE J.* 2019;65:e16684.
5. Kim CH, Qi G, Dahlberg K, Li W. Strontium-doped perovskites rival platinum catalysts for treating NO<sub>x</sub> in simulated diesel exhaust. *Science.* 2010;327:1624-1627.
6. Cheng X, Zhang X, Su D, Wang Z, Chang J, Ma C. NO reduction by CO over copper catalyst supported on mixed CeO<sub>2</sub> and Fe<sub>2</sub>O<sub>3</sub>: Catalyst design and activity test. *Appl. Catal. B.*

2018;239:485-501.

7. Heo I, You YW, Lee JH, Schmieg SJ, Yoon DY, Kim CH. Urealess NO<sub>x</sub> reduction by carbon monoxide in simulated lean-burn exhausts. *Environ. Sci. Technol.* 2020;54:8344-8351.
8. Wang L, Cheng X, Wang Z, Ma C, Qin Y. Investigation on Fe-Co binary metal oxides supported on activated semi-coke for NO reduction by CO. *Appl. Catal. B.* 2017;201:636-651.
9. Wang Y, Makkee M. The influence of CO<sub>2</sub> on NO reduction into N<sub>2</sub> over reduced ceria-based catalyst. *Appl. Catal. B.* 2018;221:196-205.
10. Cheng X, Zhang M, Sun P, Wang L, Wang Z, Ma C. Nitrogen oxides reduction by carbon monoxide over semi-coke supported catalysts in a simulated rotary reactor: reaction performance under dry conditions. *Green Chem.* 2016;18:5305-5324.
11. Qiang Y, Yao X, Zhang H, Fei G, Lin D. Effect of ZrO<sub>2</sub> addition method on the activity of Al<sub>2</sub>O<sub>3</sub>-supported CuO for NO reduction with CO: Impregnation vs. coprecipitation. *Appl. Catal. A.* 2012;423-424:42-51.
12. Tarjomannejad A, Farzi A, Niaei A, Salari D. NO reduction by CO over LaB<sub>0.5</sub>B'<sub>0.5</sub>O<sub>3</sub> (B = Fe, Mn, B' = Fe, Mn, Co, Cu) perovskite catalysts, an experimental and kinetic study. *J. Taiwan Inst. Chem. Eng.* 2017;78:200-211.
13. Silas K, Ghani WAWAK, Choong TS, Rashid U. Carbonaceous materials modified catalysts for simultaneous SO<sub>2</sub>/NO<sub>x</sub> removal from flue gas: A review. *Cat. Rev. - Sci. Eng.* 2019;61:134-161.
14. Tanabat Mudchimo SN, Nawe Kungwan, Siriporn Jungsuttiwong. Carbon-doped boron nitride nanosheet as a promising metal-free catalyst for NO reduction: DFT mechanistic study. *Appl. Catal. A.* 2018;557:79-88.
15. Damma D, Ettireddy PR, Reddy BM, Smirniotis PG. A review of low temperature NH<sub>3</sub>-SCR for removal of NO<sub>x</sub>. *Catalysts.* 2019;9:349-383.

16. Wang A, Li J, Zhang T. Heterogeneous single-atom catalysis. *Nat. Rev. Chem.* 2018;2:65-81.
17. Peng L, Wei Z. Catalyst Engineering for electrochemical energy conversion from water to water: Water electrolysis and the hydrogen fuel cell. *Engineering* 2020;6: 653-679.
18. Khivantsev K, Vargas CG, Tian J, Kovarik L, Jaegers NR, Szanyi J, Wang Y. Economizing on precious metals in three-way catalysts: Thermally stable and highly active single-atom rhodium on ceria for NO abatement under dry and industrially relevant conditions. *Angew. Chem. Int. Ed.* 2021;60:391-398.
19. Qu W, Liu X, Chen J, Dong Y, Tang X, Chen Y. Single-atom catalysts reveal the dinuclear characteristic of active sites in NO selective reduction with NH<sub>3</sub>. *Nat. Commun.* 2020;11:1532-1538.
20. Yan H, Cheng H, Yi H, Lin Y, Yao T, Wang C, Li J, Wei S, Lu J. Single-atom Pd<sub>1</sub>/graphene catalyst achieved by atomic layer deposition: Remarkable performance in selective hydrogenation of 1, 3-butadiene. *J. Am. Chem. Soc.* 2015;137:10484-10487.
21. Zhou S, Shang L, Zhao Y, Shi R, Waterhouse GIN, Huang Y-C, Zheng L, Zhang T. Pd single-atom catalysts on nitrogen-doped graphene for the highly selective photothermal hydrogenation of acetylene to ethylene. *Adv. Mater.* 2019;31:1900509-1900515.
22. Zhang J, Dai L. Nitrogen, phosphorus, and fluorine tri-doped graphene as a multifunctional catalyst for self-powered electrochemical water splitting. *Angew. Chem. Int. Ed.* 2016;55:13296-13300.
23. Lv R, Dos Santos MC, Antonelli C, Feng S, Fujisawa K, Berkdemir A, Cruz-Silva R, Elías AL, Perea-Lopez N, López-Urías F. Large-area Si-doped graphene: Controllable synthesis and enhanced molecular sensing. *Adv. Mater.* 2014;26:7593-7599.
24. Robertson AW, Montanari B, He K, Kim J, Allen CS, Wu YA, Olivier J, Neethling J, Harrison N, Kirkland AI. Dynamics of single Fe atoms in graphene vacancies. *Nano Lett.*

2013;13:1468-1475.

25. Duan J, Chen S, Jaroniec M, Qiao SZ. Heteroatom-doped graphene-based materials for energy-relevant electrocatalytic processes. *ACS Catal.* 2015;5:5207-5234.

26. Chen Y, Liu YJ, Wang HX, Zhao JX, Cai QH, Wang XZ, Ding YH. Silicon-doped graphene: An effective and metal-free catalyst for NO reduction to N<sub>2</sub>O? *ACS Appl. Mater. Interfaces.* 2013;5:5994-6000.

27. Gholizadeh R, Yu YX. N<sub>2</sub>O + CO reaction over Si- and Se-doped graphenes: An ab initio dft study. *Appl. Surf. Sci.* 2015;357:1187-1195.

28. Kresse G, Furthmüller J. Efficient iterative schemes for ab initio total-energy calculations using a plane-wave basis set. *Phys. Rev. B.* 1996;54:11169-11186.

29. Perdew JP, Burke K, Ernzerhof M. Generalized gradient approximation made simple. *Phys. Rev. Lett.* 1996;77:3865-3868.

30. Dion M, Rydberg H, Schröder E, Langreth DC, Lundqvist BI. Van der waals density functional for general geometries. *Phys. Rev. Lett.* 2004;92:246401-246404.

31. Dudarev SL, Botton GA, Savrasov SY, Humphreys CJ, Sutton AP. Electron-energy-loss spectra and the structural stability of nickel oxide: An LSDA+U study. *Phys. Rev. B.* 1998;57:1505-1509.

32. Henkelman G, Uberuaga BP, Jónsson H. A climbing image nudged elastic band method for finding saddle points and minimum energy paths. *J. Chem. Phys.* 2000;113:9901-9904.

33. Kästner J, Sherwood P. Superlinearly converging dimer method for transition state search. *J. Chem. Phys.* 2008;128:014106-014111.

34. Sprik M, Ciccotti G. Free energy from constrained molecular dynamics. *J. Chem. Phys.* 1998;109:7737-7744.

35. Wang V, Xu N, Liu J-C, Tang G, Geng W. VASPKIT: A user-friendly interface facilitating high-throughput computing and analysis using VASP code. *preprint arXiv:*

1908.08269. 2019.

36. Heyd J, Scuseria GE, Ernzerhof M. Hybrid Functionals Based on a Screened Coulomb Potential. *J. Chem. Phys.* 2003;118:8207-8215.
37. Wan W, Li H, Huang H, Wong SL, Lv L, Gao Y, Wee ATS. Incorporating isolated molybdenum (Mo) atoms into bilayer epitaxial graphene on 4H-SiC (0001). *ACS Nano.* 2014;8:970-976.
38. Liu X, Hu T, Miao Y, Ma D, Yang Z, Ma F, Xu K, Chu PK. Substitutional doping of Ag into epitaxial graphene on 6H-SiC substrates during thermal decomposition. *Carbon.* 2016;104:233-240.
39. Kirk C, Chen LD, Siahrostami S, Karamad M, Bajdich M, Voss J, Nørskov JK, Chan K. Theoretical investigations of the electrochemical reduction of CO on single metal atoms embedded in graphene. *ACS Cent. Sci.* 2017;3:1286-1293.
40. Xu H, Cheng D, Cao D, Zeng XC. A universal principle for a rational design of single-atom electrocatalysts. *Nat. Catal.* 2018;1:339-348.
41. Hibbitts D, Iglesia E. Prevalence of bimolecular routes in the activation of diatomic molecules with strong chemical bonds (O<sub>2</sub>, NO, CO, N<sub>2</sub>) on catalytic surfaces. *Acc. Chem. Res.* 2015;48:1254-1262.
42. Lietti L, Nova I, Ramis G, Dall'Acqua L, Busca G, Giamello E, Forzatti P, Bregani F. Characterization and reactivity of V<sub>2</sub>O<sub>5</sub>-MoO<sub>3</sub>/TiO<sub>2</sub> de-NO<sub>x</sub> SCR catalysts. *J. Catal.* 1999;187:419-435.
43. Lietti L, Forzatti P. Temperature programmed desorption/reaction of ammonia over V<sub>2</sub>O<sub>5</sub>/TiO<sub>2</sub> de-NO<sub>x</sub>ing catalysts. *J. Catal.* 1994;147:241-249.
44. Tang S, Dang Q, Liu T, Zhang S, Zhou Z, Li X, Wang X, Sharman E, Luo Y, Jiang J. Realizing a Not-Strong-Not-Weak Polarization Electric Field in Single-Atom Catalysts Sandwiched by Boron Nitride and Graphene Sheets for Efficient Nitrogen Fixation. *J. Am.*

*Chem. Soc.* 2020;142:19308-19315.



## Figure Captions

**Figure 1** (a) Atomic structure of the single-atom-doped graphene (SADGr) catalyst. (b) Cohesive energies of SADGr sheets with different dopants respecting to bulk (black splines) and single atomic (red splines) forms. (c) Schematic illustration for the reaction cycles (left panel) and the possible elementary steps (left panel) in the  $\text{NO}_x$  reduction by CO on SADGr surfaces. The D in the skeletal formulas represents the active site of the doped atom. It should be noted that step v can be divided into v(i) and v(ii), and step viii may be divided to viii(i) and viii(ii) on some SADGr surfaces.

**Figure 2.** (a, b) The adsorption free energies of the key surface species on the SADGr surfaces; (c) the reaction free energy barriers of the elementary steps on the SADGr surfaces.

**Figure 3.** Gibbs free energy profiles of NO reduction to  $\text{N}_2\text{O}$  and  $\text{O}^*$  on the SADGr surfaces at 450 K and 1 atm. The paths depicted by the red lines are the optimal paths, which are chosen to do the microkinetic analysis. The structures (D2 and D3) within the areas filled with mosaic frames can be transformed to each other with very low energy barriers.

**Figure 4.** Gibbs free energy profiles of  $\text{NO}_2$  reduced by CO to  $\text{NO}^*$  and  $\text{CO}_2$  on the SADGr surfaces at 450 K and 1 atm. The paths depicted by the red lines are the optimal paths, which are chosen to do microkinetic analysis. The structures within the areas filled with mosaic frames can be transformed to each other with very low energy barriers.

**Figure 5.** Gibbs free energy profiles of  $\text{N}_2\text{O}$  reduction to  $\text{O}^*$  and  $\text{N}_2$  on the SADGr surfaces at 450 K and 1 atm.

**Figure 6.** Gibbs free energy profiles of CO oxidation by  $\text{O}^*$  on the SADGr surfaces after at 450 K and 1 atm.

**Figure 7.** (a) The TOFs of key steps iii, v, vii, and viii on the SADGr surfaces. (b) The normalized occupancy concentrations of possible surface species from

microkinetic analysis. **(c)** The TOFs of step viii on TiGr at 450 K respecting to the NO and CO partial pressures. **(d)** The TOFs of steps iii, v, vii, and viii catalyzed by CoGr versus the CO partial pressure ( $T = 450\text{ K}$ ;  $P_{\text{NO}} = 1.01\text{ Pa}$ , 10 ppm;  $P_{\text{N}_2\text{O}} = 101.33\text{ Pa}$ , 1000 ppm).

**Figure 8.** The consistency between the reaction free energy barriers and the descriptors combined by adsorption free energies and atomic electronegativities in the reactions of **(a)** NO reduction (steps i, ii and iii), **(b)** NO<sub>2</sub> reduction (step iv and v), **(c)** N<sub>2</sub>O reduction (steps vi and vii), and **(d)** CO oxidation (step viii), respectively.

**Figure 9.** Values of  $|\Delta G_{\text{ads}}|$  versus the Bader charges of the doping atoms in the adsorption structures of **(a)** NO-ads1, **(b)** CO-ads1, **(c)** NO<sub>2</sub>-ads3 and **(d)** O\*, respectively. The data points circled in red are excluded for the derivation of the relationships. The legends show the linear change trend of the adsorption free energy and the Bader charge. **(e)** The Bader charges of the single atoms doped in SADGr.